INTERNATIONAL JOURNAL FOR NUMERICAL METHODS IN FLUIDS
Int. J. Numer. Meth. Fluids (2012)
Published online in Wiley Online Library (wileyonlinelibrary.com/journal/nmf). DOI: 10.1002/fld.3734

A collocated grid, projection method for time-accurate calculation of low-Mach number variable density flows in general curvilinear coordinates

Mahdi Kooshkbaghi[1] and Bamdad Lessani[2,*,†]

[1]*Aerothermochemistry and Combustion Systems Laboratory, Swiss Federal Institute of Technology, Zurich CH-8092, Switzerland*
[2]*Mechanical and Industrial Engineering Department, University of Toronto, 5 King's College Road, Toronto, ON, Canada M5S 3G8*

SUMMARY

A time-accurate algorithm is proposed for low-Mach number, variable density flows on curvilinear grids. Spatial discretization is performed on collocated grid that offers computational simplicity in curvilinear coordinates. The flux interpolation technique is used to avoid the pressure odd–even decoupling of the collocated grid arrangement. To increase the stability of the method, a two-step predictor–corrector time integration scheme is employed. At each step, the projection method is used to calculate the hydrodynamic pressure and to satisfy the continuity equation. The robustness and accuracy of the method is illustrated with a series of numerical experiments including thermally driven cavity, polar cavity, three-dimensional cavity, and direct numerical simulation of non-isothermal turbulent channel flow. Copyright © 2012 John Wiley & Sons, Ltd.

Received 13 April 2012; Revised 25 July 2012; Accepted 28 August 2012

KEY WORDS: variable density; low Mach number approximation; curvilinear grids; projection; collocated grid

1. INTRODUCTION

Time-accurate calculation of low-Mach number, variable density flows has important applications in technological processes and natural phenomena. Time-accurate variable density solvers may be used in large-eddy or direct numerical simulations of turbulent flames, convection with large temperature differences, and in the numerical simulations of meteorological and atmospheric flows.

Two general strategies may be employed for time-accurate calculations of low-Mach number flows. The first one is to use the unsteady preconditioning technique in a compressible solver and to substitute the physical speed of sound by a preconditioned speed of sound. In this method, the maximum time step of the solver is not limited by the acoustic wave speed, and a time-accurate calculation may be possible in a reasonable computational time ([1–4]). Lessani *et al.* [4] reported that applying unsteady preconditioning technique combined with multigrid and residual smoothing could decrease the computational time of an explicit compressible large-eddy simulation solver by up to a factor of 7. The efficiency gain, however, largely depends on the non-uniformity and the clustering of the computational mesh, and also on the physical time step of the flow field, and it may drop considerably if these parameters are not carefully chosen.

The second strategy, which relies on the projection method, is based on the low-Mach number approximation of the Navier–Stokes equations [5]. Charentenay *et al.* [6] compared the

*Correspondence to: Bamdad Lessani, Mechanical and Industrial Engineering Department, University of Toronto, 5 King's College Road, Toronto, ON, Canada M5S 3G8.

†E-mail: bamdad.lessani@gmail.com

computational time of a compressible solver with that of a low-Mach solver, and they concluded that the computing time associated with the low-Mach solver is at least one order of magnitude shorter than that of a compressible solver for the simulation of turbulent flames. In their study, they considered the interaction of turbulence with an initially laminar premixed ozone flame, and they reported that the limiting time step of the compressible solver was $\Delta t = 2.6 \times 10^{-8}$ (s) corresponding to the classical acoustic Courant Friedrichs Lewy (CFL) limitation, whereas the time step of the low-Mach solver was $\Delta t = 2 \times 10^{-7}$ (s), limited by the diffusion stability condition. The overall computing time of the compressible solver was 11 times higher than the computing time of the low-Mach solver.

Although the low-Mach number approximation is known to be an efficient method for the simulation of variable density flows, there are two main issues that need to be carefully addressed in this method. The first issue is the instability of this method at high-temperature differences, and the second issue is the odd–even decoupling of the pressure field.

Regarding the first issue, different techniques have been adopted to increase the robustness of the projection method at high-temperature differences ([7–15]). Cook and Riley [7] reported that their numerical algorithm was stable for temperature variations up to about a factor of 3. Najm *et al.* [8] proposed a predictor–corrector method to increase the robustness of their algorithm. Nicoud [10] reported an algorithm on the basis of a mixed Runge–Kutta/Crank–Nicolson time stepping and a variable coefficient Poisson equation for the pressure to increase the stability of the method. Lessani and Papalexandris [11, 12] applied a two-stage predictor–corrector time marching scheme for flows with strong temperature gradients on Cartesian collocated grids. Pierce [13] and Sewall and Tafti [14] used iterative approaches in their simulations to make their algorithm stable at large temperature differences.

The second important issue is the odd–even decoupling of the pressure field. To avoid this problem, Harlow and Welch [16] proposed the staggered grid arrangement, which can be easily applied to two-dimensional incompressible flows, but it becomes very complex to implement for three-dimensional variable density flows in curvilinear coordinates.

An alternative to the staggered grid arrangement is the collocated grid arrangement. The majority of the studies reported in the literature, however, are limited to the incompressible flow simulations. To name a few, Zang *et al.* [17] employed a non-staggered (collocated) grid for incompressible flow simulation in curvilinear coordinates and extended the flux interpolation technique of Rhie and Chow [18] to unsteady flows. Morinishi *et al.* [19] studied the kinetic energy conservation properties of collocated grids for large-eddy simulation of turbulent flows. Armenio and Piomelli [20] introduced a subgrid scale model for large-eddy simulation of incompressible flow on collocated non-orthogonal meshes. Moulinec and Wesseling [21] compared the accuracy of different finite volume schemes on collocated curvilinear grids. Jothiprasad and Caughey [22] introduced a fractional-step method for large-eddy simulation of incompressible flow on non-uniform collocated grids. Gopalakrishnan and Tafti [23] proposed a numerical procedure for unsteady incompressible flow simulation on a collocated finite-volume multiblock grid in general curvilinear coordinates.

There are fewer studies on the time-accurate calculations of variable density low-Mach number flows on collocated grids. The study of Rauwoens *et al.* [15] is among the few studies that use a collocated grid arrangement in curvilinear coordinates for low-Mach number variable density flows. They obtained the pressure Poisson equation from a combination of the continuity and energy equations, and they carefully treated the conductive terms of the energy equation to assure the solvability of the pressure Poisson equation.

In the present article, we describe a robust and easy-to-implement algorithm for time-accurate calculation of variable density low-Mach number flows in complex geometries. The two issues of low-Mach number solvers, namely, the instability at high-temperature differences and the pressure odd–even decoupling, have been carefully addressed. To increase the stability of the scheme at high-temperature differences, a two-stage predictor–corrector time marching method, which its robustness has been previously assessed [11, 12, 24], is employed. To avoid the problem of pressure odd–even decoupling, the flux interpolation technique [18, 19] is generalized herein to variable density flows in curvilinear grids. The algorithm is based on the extension of the non-staggered grid fractional step method of Zang *et al.* [17] to low-Mach number variable density flows.

DOI: 10.1002/fld

The article is organized as follows. The governing equations are described in Section 2. The numerical method including the spatial and temporal discretizations are described in detail in Section 3. Section 4 contains the results of the numerical simulations. General conclusions are drawn in Section 5.

2. MATHEMATICAL FORMULATION

After the low–Mach number approximation is applied to the continuity, momentum, energy, and ideal gas law equations, they may be written as [5]

$$\frac{\partial \rho}{\partial t} + \frac{\partial \rho u_i}{\partial x_i} = 0 \tag{1}$$

$$\frac{\partial \rho u_i}{\partial t} + \frac{\partial \rho u_i u_j}{\partial x_j} = -\frac{\partial p^{(1)}}{\partial x_i} + \frac{1}{Re}\frac{\partial \sigma_{ij}}{\partial x_j} - \frac{\rho \delta_{i2}}{Fr^2} \tag{2}$$

$$\rho c_p \frac{\partial T}{\partial t} + \rho c_p u_j \frac{\partial T}{\partial x_j} = \frac{1}{RePr}\frac{\partial}{\partial x_j}\left(\kappa \frac{\partial T}{\partial x_j}\right) + \frac{\gamma - 1}{\gamma}\frac{\mathrm{d}p^{(0)}}{\mathrm{d}t} \tag{3}$$

$$p^{(0)} = \rho T\,, \quad \text{and} \quad \frac{\partial p^{(0)}}{\partial x_i} = 0 \tag{4}$$

The viscous stress tensor σ_{ij} is given by

$$\sigma_{ij} = \mu\left(\frac{\partial u_i}{\partial x_j} + \frac{\partial u_j}{\partial x_i} - \frac{2}{3}\delta_{ij}\frac{\partial u_k}{\partial x_k}\right) \tag{5}$$

In the aforementioned equations, x_i, t, ρ, u_i, T, denote the ith spatial coordinate, time, density, ith velocity vector component, and temperature, respectively. The pressure field is decomposed into a spatially uniform component $p^{(0)}$, interpreted as the thermodynamic pressure, and a variable component $p^{(1)}$, interpreted as the hydrodynamic pressure. The hydrodynamic pressure $p^{(1)}$ can be calculated by a projection method leading to a Poisson equation for the pressure. With regards to the evolution of $p^{(0)}$, in case of an open system, $p^{(0)}$ is constant and equal to the open boundary pressure. For a closed system, $p^{(0)}$ may vary in time, and by integrating the equation $p^{(0)} = \rho T$ over the volume of the system V, the following expression is readily obtained

$$p^{(0)} = \frac{M_0}{\int \frac{\mathrm{d}V}{T^{(0)}}} \tag{6}$$

with M_0 the total mass of the closed system.

The Prandtl and Reynolds numbers are defined with respect to the following references values: $Pr = \mu(T_{\mathrm{ref}})\, c_p(T_{\mathrm{ref}})/\kappa(T_{\mathrm{ref}})$, $Re = \rho_{\mathrm{ref}}\, u_{\mathrm{ref}}\, L_{\mathrm{ref}}/\mu(T_{\mathrm{ref}})$. For problems with high-temperature differences, the Sutherland law may be used for the dimensionless thermal conductivity κ and dynamic viscosity μ, whereas the specific heat c_p is assumed to be constant. The last term in Equation (2), $\rho\delta_{i2}/Fr^2$, is the gravitational acceleration in the negative y direction, in which the Froude number is defined as $Fr = u_{\mathrm{ref}}/\sqrt{g L_{\mathrm{ref}}}$, and $1/Fr^2$ is interpreted as the ratio of gravity to inertia forces.

To transform the governing equations from a Cartesian x_i to a curvilinear ξ_i system of coordinates, the generalized coordinate transformation method (see, e.g., [25]) can be used. With the use of the chain rule, the continuity equation can be recast as

$$J^{-1}\frac{\partial \rho}{\partial t} + \frac{\partial \rho U_i}{\partial \xi_i} = 0 \tag{7}$$

with

$$U_i = u_j \frac{\partial \xi_i}{\partial x_j} J^{-1}\,, \quad \text{and} \quad J^{-1} = \det\left(\frac{\partial x_i}{\partial \xi_j}\right) \tag{8}$$

DOI: 10.1002/fld

The momentum Equation (2) in curvilinear coordinate system ξ_i may be written as

$$J^{-1}\frac{\partial \rho u_i}{\partial t} + \underbrace{\frac{\partial \rho U_m u_i}{\partial \xi_m}}_{Convu_i} = -\underbrace{\frac{\partial}{\partial \xi_m}\left(J^{-1}\frac{\partial \xi_m}{\partial x_i}p^{(1)}\right)}_{Gradpu_i} + \underbrace{\frac{1}{Re}\frac{\partial}{\partial \xi_m}\left(J^{-1}\sigma_{ij}\frac{\partial \xi_m}{\partial x_j}\right)}_{Viscu_i} - \frac{J^{-1}\rho\delta_{i2}}{Fr^2} \tag{9}$$

with $Convu_i$, $Gradpu_i$, and $Viscu_i$, the convective, pressure gradient, and viscous terms, respectively. The governing equation for U_j can be obtained by multiplying both sides of Equation (9) by $\partial \xi_j / \partial x_i$

$$\frac{\partial \rho U_j}{\partial t} + \underbrace{\frac{\partial \xi_j}{\partial x_i}\frac{\partial \rho U_m u_i}{\partial \xi_m}}_{ConvU_j} = -\underbrace{L_{mj}\frac{\partial p^{(1)}}{\partial \xi_m}}_{GradpU_j} + \underbrace{\frac{1}{Re}\frac{\partial \xi_j}{\partial x_i}\frac{\partial}{\partial \xi_m}\left(J^{-1}\sigma_{il}\frac{\partial \xi_m}{\partial x_l}\right)}_{ViscU_j} - \frac{\partial \xi_j}{\partial x_2}\frac{J^{-1}\rho}{Fr^2} \tag{10}$$

with L_{mj} the mesh skewness factor defined as

$$L_{mj} = J^{-1}\frac{\partial \xi_m}{\partial x_i}\frac{\partial \xi_j}{\partial x_i} \tag{11}$$

where $ConvU_j$, $GradpU_j$, and $ViscU_j$ are the convective, pressure gradient, and viscous terms, respectively.

Finally, the energy Equation (3) in curvilinear coordinate system may be written as

$$\rho c_p \frac{\partial T}{\partial t} + \underbrace{\rho c_p u_i \frac{\partial T}{\partial \xi_m}\frac{\partial \xi_m}{\partial x_i}}_{ConvT} = \underbrace{\frac{1}{RePr}\frac{\partial}{\partial \xi_m}\left(k\frac{\partial T}{\partial \xi_n}\frac{\partial \xi_n}{\partial x_i}\right)\frac{\partial \xi_m}{\partial x_i}}_{ViscT} + \frac{\gamma - 1}{\gamma}\frac{\mathrm{d}p^{(0)}}{\mathrm{d}t} \tag{12}$$

with $ConvT$ and $ViscT$ the convective and viscous terms, respectively.

3. NUMERICAL METHOD

For the spatial discretization of the governing Equations (7–12), a collocated grid system is used with u_i, U_i, and p all stored at the center of the computational cell. Compared with the staggered grid system, the discretization of the viscous terms in Equations (9–12) is much simpler in a collocated grid system. To prevent the odd–even decoupling of the pressure typically encountered in collocated grids, the convective term is discretized using an auxiliary flux F_i, defined at the cell faces. A sketch of the grid layout in two-dimension is shown in Figure 1. In the following, it is described how the convective and the viscous terms as well as the auxiliary fluxes F_i are calculated.

3.1. Spatial discretization

The general finite difference operator acting on $\phi(\xi_1, \xi_2, \xi_3)$ in the ξ_1 direction is defined as

$$\frac{\delta_n \phi(\xi_1, \xi_2, \xi_3)}{\delta_n \xi_1} = \frac{\phi\left(\xi_1 + n\frac{\Delta\xi_1}{2}, \xi_2, \xi_3\right) - \phi\left(\xi_1 - n\frac{\Delta\xi_1}{2}, \xi_2, \xi_3\right)}{n\Delta\xi_1} \tag{13}$$

with $\Delta\xi_1$ the grid spacing in the ξ_1 direction. Similar definitions hold for operators acting in the ξ_2 and ξ_3 directions. The grid spacing in the computational domain is taken equal to one, i.e., $\Delta\xi_i = 1$.

The general interpolation operator acting in the ξ_1 direction is defined as

$$\overline{\phi}^{\xi_1}(\xi_1, \xi_2, \xi_3) = \frac{\phi\left(\xi_1 + \frac{\Delta\xi_1}{2}, \xi_2, \xi_3\right) + \phi\left(\xi_1 - \frac{\Delta\xi_1}{2}, \xi_2, \xi_3\right)}{2} \tag{14}$$

with similar definitions for operators acting in the other two spatial directions.

DOI: 10.1002/fld

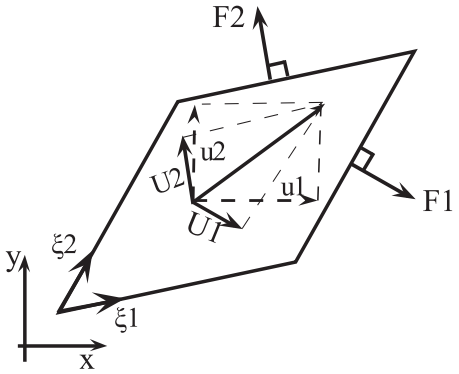

Figure 1. Collocated grid with u_i, U_i, and p defined at the cell center, and F_i defined at the cell faces. The components of u_i, U_i, and F_i are schematically shown.

3.1.1. Convective terms. The convective term $Convu_i$ in the momentum Equation (9) can be approximated as

$$Convu_i \equiv \frac{\partial \rho U_m u_i}{\partial \xi_m} \simeq \frac{\delta_1 F_m \overline{u_i}^{\xi_m}}{\delta_1 \xi_m} \tag{15}$$

The summation convention does not apply to the ξ_m appearing as a superscript. To update the auxiliary flux F_i in Equation (15), the momentum equation is discretized at the face of the computational cell. With the use of a first-order time marching method with the known values at time level n, the new cell face values of F_i^{n+1} at time level $n+1$ can be calculated from Equation (10) as

$$F_i^{n+1} = \overline{\rho^n U_i^n}^{\xi_i} + \Delta t \left(\overline{ViscU_i^n}^{\xi_i} - \overline{ConvU_i^n}^{\xi_i} - GradpU_i \right) \tag{16}$$

At each face, the cell face values of $\overline{ViscU_i^n}^{\xi_i}$ and $\overline{ConvU_i^n}^{\xi_i}$ are obtained by averaging the cell-centered values of the neighboring cells. The pressure gradient $GradpU_i$ is directly discretized at the cell face using the pressure stored at the cell centers. The sum of the three terms at the right hand side of Equation (16), divided by the density, is typically called the intermediate velocity in the projection method. For buoyant flows, the gravitational acceleration term in Equation (10) should also be added to the sum of the viscous and convective residuals in Equation (16).

For time-accurate calculations, instead of a first-order time marching method in Equation (16), a second-order Adams–Bashforth is used to update the values of F_i, u_i, and U_i in the momentum equations. This issue will be further explained in Section 3.2.1.

The discrete form of the convective term $ConvU_j$ in the momentum Equation (10) is obtained by multiplying the metrics $\partial \xi_j / \partial x_i$ by Equation (15)

$$ConvU_j \equiv \frac{\partial \xi_j}{\partial x_i} \frac{\partial \rho U_m u_i}{\partial \xi_m} \simeq \left(\frac{\partial \xi_j}{\partial x_i} \right)_{\text{c.c}} \frac{\delta_1 F_m \overline{u_i}^{\xi_m}}{\delta_1 \xi_m} \tag{17}$$

with $(\partial \xi_j / \partial x_i)_{c.c}$ the value of the metrics at the cell center. The metrics are initially evaluated at the corner nodes of the computational grid. For two-dimensional flows, the metrics at the cell centers are calculated as the average of the four neighboring corner nodes, and for three-dimensional flows, the eight neighboring corner nodes are considered.

The convective term $ConvT$ of the energy Equation (12) is approximated as

$$ConvT \equiv \rho c_p u_i \frac{\partial T}{\partial \xi_m} \frac{\partial \xi_m}{\partial x_i} \simeq \rho c_p \left(\overline{\bar{u_i}^{\xi_m} \frac{\delta_1 T}{\delta_1 \xi_m}}^{\xi_m} \right) \left(\frac{\partial \xi_m}{\partial x_i} \right)_{\text{c.c}} \tag{18}$$

DOI: 10.1002/fld

3.1.2. Pressure gradient terms. The pressure gradient term $Gradpu_i$ of the momentum Equation (9) at the cell center may be discretized as

$$Gradpu_i \equiv \frac{\partial}{\partial \xi_m}\left(J^{-1}\frac{\partial \xi_m}{\partial x_i}p^{(1)}\right) \simeq \frac{\partial}{\partial \xi_m}\left(\left(J^{-1}\right)_{\text{c.f}}\left(\frac{\partial \xi_m}{\partial x_i}\right)_{\text{c.f}}\overline{p^{(1)}}^{\xi_m}\right) \tag{19}$$

Similarly, in Equation (10), the pressure gradient $GradpU_j$ at the cell center is obtained from multiplying the metrics $(\partial \xi_j/\partial x_i)_{\text{c.c}}$ by Equation (19)

$$GradpU_j = L_{mj}\frac{\partial p^{(1)}}{\partial \xi_m} \simeq L_{mj_{\text{c.c}}}\frac{\delta_2 p^{(1)}}{\delta_2 \xi_m} = \left(J^{-1}\right)_{\text{c.c}}\left(\frac{\partial \xi_m}{\partial x_i}\right)_{\text{c.c}}\left(\frac{\partial \xi_j}{\partial x_i}\right)_{\text{c.c}}\frac{\delta_2 p^{(1)}}{\delta_2 \xi_m} \tag{20}$$

On the other hand, if $GradpU_j$ is to be discretized at the cell face, for example to update the flux F_j in Equation (16), the discrete pressure gradient may be written as

$$GradpU_j = L_{mj}\frac{\partial p^{(1)}}{\partial \xi_m} \simeq L_{mj_{\text{c.f}}}\frac{\delta_1 p^{(1)}}{\delta_1 \xi_m} = \left(J^{-1}\right)_{\text{c.f}}\left(\frac{\partial \xi_m}{\partial x_i}\right)_{\text{c.f}}\left(\frac{\partial \xi_j}{\partial x_i}\right)_{\text{c.f}}\frac{\delta_1 p^{(1)}}{\delta_1 \xi_m} \tag{21}$$

In Equations (19) and (21), $(J^{-1})_{\text{c.f}}$ and $(\partial \xi_m/\partial x_i)_{\text{c.f}}$, $(\partial \xi_j/\partial x_i)_{\text{c.f}}$ are the Jacobian and the metrics at the face of the computational cell. In two-dimension, the cell face values of the metrics are the average of the two neighboring corner nodes, and in three-dimension, they are the average of the four neighboring corner nodes. Having computed the metrics, the cell face values of the Jacobian are readily calculated.

3.1.3. Viscous terms. All viscous terms in the momentum and energy equations are approximated with a central second-order finite difference method, and they are all evaluated at the center of the computational cell.

In the momentum Equation (9), the viscous term $Viscu_i$ may be written as

$$\begin{aligned} Re\cdot Viscu_i &\equiv \frac{\partial}{\partial \xi_m}\left(J^{-1}\mu\left(\frac{\partial u_i}{\partial \xi_p}\frac{\partial \xi_p}{\partial x_j}+\frac{\partial u_j}{\partial \xi_p}\frac{\partial \xi_p}{\partial x_i}-\frac{2}{3}\delta_{ij}\frac{\partial u_k}{\partial \xi_p}\frac{\partial \xi_p}{\partial x_k}\right)\frac{\partial \xi_m}{\partial x_j}\right)\\ &\simeq \frac{\delta_1}{\delta_1 \xi_m}\left(\overline{\mu}^{\xi_m}\left(J^{-1}\right)_{\text{c.f}}\left(\frac{\partial \xi_m}{\partial x_j}\right)_{\text{c.f}}\left(\frac{\partial \xi_p}{\partial x_j}\right)_{\text{c.f}}\frac{\delta_1 u_i}{\delta_1 \xi_p}\right)\\ &\quad+\frac{\delta_1}{\delta_1 \xi_m}\left(\overline{\mu}^{\xi_m}\left(J^{-1}\right)_{\text{c.f}}\left(\frac{\partial \xi_m}{\partial x_j}\right)_{\text{c.f}}\left(\frac{\partial \xi_p}{\partial x_i}\right)_{\text{c.f}}\frac{\delta_1 u_j}{\delta_1 \xi_p}\right)\\ &\quad-\frac{2}{3}\delta_{ij}\frac{\delta_1}{\delta_1 \xi_m}\left(\overline{\mu}^{\xi_m}\left(J^{-1}\right)_{\text{c.f}}\left(\frac{\partial \xi_m}{\partial x_j}\right)_{\text{c.f}}\left(\frac{\partial \xi_p}{\partial x_k}\right)_{\text{c.f}}\frac{\delta_1 u_k}{\delta_1 \xi_p}\right) \end{aligned} \tag{22}$$

Similarly, in the momentum Equation (10), the viscous term $ViscU_j$ is obtained by multiplying the metrics $(\partial \xi_j/\partial x_i)_{\text{c.c}}$ by Equation (22).

Finally, the viscous term $ViscT$ of the energy Equation (12) can be approximated as

$$Re\cdot Pr\cdot ViscT \equiv \frac{\partial}{\partial \xi_m}\left(k\frac{\partial T}{\partial \xi_n}\frac{\partial \xi_n}{\partial x_i}\right)\frac{\partial \xi_m}{\partial x_i} \simeq \left(\frac{\partial \xi_m}{\partial x_i}\right)_{\text{c.c}}\frac{\delta_1}{\delta_1 \xi_m}\left(\overline{k}^{\xi_m}\left(\frac{\partial \xi_n}{\partial x_i}\right)_{\text{c.f}}\frac{\delta_1 T}{\delta_1 \xi_n}\right) \tag{23}$$

3.1.4. Pressure Poisson equation. In the projection method, the pressure $p^{(1)}$ is calculated by taking the divergence of the momentum equation leading to a Poisson equation for the pressure. For the discrete equations, special care should be taken to avoid the typical odd–even decoupling problem of the pressure field. In view of this, the discrete divergence operator is applied to the momentum Equation (16) leading to

$$\frac{\delta_1 F_i^{n+1}}{\delta_1 \xi_i} = \frac{\delta_1}{\delta_1 \xi_i}\overline{(\rho U_i)^*}^{\xi_i} - \Delta t\frac{\delta_1}{\delta_1 \xi_i}\left(L_{mi_{\text{c.f}}}\frac{\delta_1 p^{(1)}}{\delta_1 \xi_m}\right) \tag{24}$$

DOI: 10.1002/fld

In the aforementioned equation, $\overline{(\rho U_i)^*}^{\xi_i}$ is the sum of the first three terms on the right hand side of Equation (16) and may be called the intermediate flux. The pressure gradient $\delta_1 p^{(1)}/\delta_1 \xi_m$ is evaluated at the face of the computational cell.

Furthermore, if the continuity Equation (7) is written in terms of the flux F_i, the left hand side of Equation (24) can be replaced by the time derivative of the density, which, with a second-order backward discretization may be written as,

$$\frac{3\rho^{n+1} - 4\rho^n + \rho^{n-1}}{J2\Delta t} + \frac{\delta_1}{\delta_1 \xi_i}\overline{(\rho U_i)^*}^{\xi_i} = \Delta t \frac{\delta_1}{\delta_1 \xi_i}\left(L_{mi_{\mathrm{c.f}}} \frac{\delta_1 p^{(1)}}{\delta_1 \xi_m}\right) \tag{25}$$

3.2. Temporal discretization

The general structure of the time integration predictor–corrector scheme in curvilinear grids is similar to the one of the Cartesian grids [11]. In this section, we describe the predictor–corrector scheme in curvilinear grids. Superscripts n, $*$, and $n+1$ denote the known values at the time level n, the predicted values, and the values at the next time level, respectively. The time step is Δt, with $t_{n+1} = t_n + \Delta t$.

3.2.1. Predictor

1. From Equation (12), the predicted temperature T^* is evaluated from the known values at time level n
$$\rho^n c_p \frac{T^* - T^n}{\Delta t} = Res_T(\rho^n, u_i^n, T^n) + \frac{\gamma - 1}{\gamma}\frac{p^{(0)n} - p^{(0)n-1}}{\Delta t} \tag{26}$$
with $Res_T = -ConvT + ViscT$, the sum of the convective and viscous residuals in Equation (12). The convective and viscous terms are discretized according to Equations (18) and (23), respectively.
2. If the system is open, the pressure $p^{(0)*}$ is constant and equal to the open boundary pressure. If the system is closed, $p^{(0)*}$ is calculated from the predicted temperature using Equation (6).
3. The predicted density ρ^* is calculated from Equation (4); $\rho^* = p^{(0)*}/T^*$.
4. The predicted flux $(\rho U_i)^*$ is calculated using an Adams–Bashforth method for the convective and viscous residuals
$$(\rho U_i)^* = \rho^n U_i^n + \Delta t\left(\frac{3}{2}Res_U(\rho^n, u_i^n, U_i^n) - \frac{1}{2}Res_U\left(\rho^{n-1}, u_i^{n-1}, U_i^{n-1}\right)\right) \tag{27}$$
where $Res_U = -ConvU_i + ViscU_i$ is the sum of the convective and viscous terms in Equation (10). For buoyant flows, the gravitational acceleration term should also be added to Res_U.
5. The predicted hydrodynamic pressure $p^{(1)*}$ is calculated from the Poisson equation
$$\frac{3\rho^* - 4\rho^n + \rho^{n-1}}{J2\Delta t} + \frac{\delta_1}{\delta_1 \xi_i}\overline{(\rho U_i)^*}^{\xi_i} = \Delta t \frac{\delta_1}{\delta_1 \xi_i}\left(L_{mi_{\mathrm{c.f}}} \frac{\delta_1 p^{(1)*}}{\delta_1 \xi_m}\right) \tag{28}$$
6. The predicted velocity u_i^* is calculated from Equation (9)
$$\rho^* u_i^* = \rho^n u_i^n + J\Delta t\left(\frac{3}{2}Res_u(\rho^n, u_i^n, U_i^n) - \frac{1}{2}Res_u(\rho^{n-1}, u_i^{n-1}, U_i^{n-1}) - Gradpu_i\right) \tag{29}$$
with $Res_u = -Convu_i + Viscu_i$, the sum of the convective and viscous residuals in Equation (9). For buoyant flows, the gravitational acceleration term should also be added to Res_u.

3.2.2. Corrector

1. The temperature at the new time level, T^{n+1}, is calculated on the basis of the values computed at the predictor stage
$$\rho^* c_p \frac{T^{n+1} - T^n}{\Delta t} = Res_T(\rho^*, u_i^*, T_{\mathrm{av}}) + \frac{\gamma - 1}{\gamma}\frac{p^{(0)n} - p^{(0)n-1}}{\Delta t} \tag{30}$$
with $T_{\mathrm{av}} = (T^n + T^*)/2$.

DOI: 10.1002/fld

2. If the system is open, the pressure $p^{(0)}$ is constant and equal to the open boundary pressure. If the system is closed, $p^{(0)n+1}$ is calculated from the predicted temperature using Equation (6).
3. The density ρ^{n+1} at time level $n+1$ is calculated from Equation (4); $\rho^{n+1} = p^{(0)n+1}/T^{n+1}$.
4. The pressure $p^{(1)n+1}$ is calculated from the Poisson equation

$$\frac{3\rho^{n+1} - 4\rho^n + \rho^{n-1}}{J2\Delta t} + \frac{\delta_1}{\delta_1 \xi_i}\overline{(\rho U_i)^*}^{\xi_i} = \Delta t \frac{\delta_1}{\delta_1 \xi_i}\left(L_{mi_{\mathrm{c.f}}} \frac{\delta_1 p^{(1)n+1}}{\delta_1 \xi_m}\right) \tag{31}$$

The $(\rho U_i)^*$ term has already been calculated in Equation (27) at the cell center, and $\overline{(\rho U_i)^*}^{\xi_i}$ may be evaluated at the cell face using the linear interpolation.
5. The velocity u_i^{n+1} is calculated from Equation (9)

$$\rho^{n+1}u_i^{n+1} = \rho^n u_i^n + J\Delta t\left(\frac{3}{2}Res_u\left(\rho^n, u_i^n, U_i^n\right) - \frac{1}{2}Res_u\left(\rho^{n-1}, u_i^{n-1}, U_i^{n-1}\right) - Gradpu_i\right) \tag{32}$$

6. The velocity U_i^{n+1} is obtained from Equation (8)

$$U_i^{n+1} = u_j^{n+1}\frac{\partial \xi_i}{\partial x_j}J^{-1} \tag{33}$$

7. The flux F_i^{n+1} is updated as

$$F_i^{n+1} = \overline{(\rho U_i)^*}^{\xi_i} - \Delta t\, GradpU_i \tag{34}$$

The pressure gradient $GradpU_i$ is determined at the cell face according to Equation (21).
9. If the temperature variations are high, to increase the stability of the scheme, the temperature equation may be reintegrated from time t_n to t_{n+1} with the final values of the density and velocity

$$\rho^{n+1}c_p\frac{T^* - T^n}{\Delta t} = Res_T(\rho^{n+1}, u_i^{n+1}, T^n) + \frac{\gamma - 1}{\gamma}\frac{p^{(0)n} - p^{(0)n-1}}{\Delta t} \tag{35}$$

$$\rho^{n+1}c_p\frac{T^{n+1} - T^n}{\Delta t} = Res_T(\rho^{n+1}, u_i^{n+1}, T_{\mathrm{av}}) + \frac{\gamma - 1}{\gamma}\frac{p^{(0)n} - p^{(0)n-1}}{\Delta t} \tag{36}$$

with $T_{\mathrm{av}} = (T^n + T^*)/2$.

4. RESULTS

Five test cases are considered to test the ability of the algorithm. First, to assess the capability of the algorithm in modeling the variable density flows, the numerical solutions of natural convection in two-dimensional square cavity with large horizontal temperature difference are compared with the benchmark solutions of Vierendeels *et al.* [26]. The second test case is the thermally driven flow in an inclined cavity with an inclination angle of 45°, used as a benchmark test problem for non-orthogonal grids (Demirdzic *et al.* [27] and Cheng *et al.* [28]). Next, the incompressible lid-driven polar cavity is considered, and the results are compared with the experimental data of Fuchs and Tillmark [29] and the numerical results of Zang *et al.* [17]. For the fourth case, the numerical results of three-dimensional cavity on a non-uniform Cartesian grid are compared with the simulation of Albensoeder and Kuhlmann [30] obtained with a Chebyshev spectral method. Finally, direct numerical simulation of non-isothermal turbulent channel flow on distorted mesh is considered as a three-dimensional unsteady problem, and the results are compared with the direct numerical simulation of Nicoud and Poinsot [31, 32]. In addition to the cases mentioned previously, the uniform flow on a curvilinear grid has also been tested (results not presented) to ensure that the solver preserves a uniform flow, and it is free of the geometrically induced errors arising from the discretization of the metric terms.

DOI: 10.1002/fld

4.1. Thermally driven square cavity

A square cavity is considered with insulated top and bottom walls, and isothermal vertical side walls as shown in Figure 2. The left wall is kept at a temperature of T_h, and the right wall is at a temperature of T_c. The average temperature T_0 is defined as $T_0 = (T_h + T_c)/2$, and the non-dimensional temperature difference parameter is represented by $\epsilon = (T_h - T_c)/(2T_0)$. The steady state results are compared with the data of Vierendeels *et al.* [26] for $\epsilon = 0.4$ and the Rayleigh number of

$$Ra = Pr\frac{g\rho_0^2(T_h - T_c)L^3}{T_0\mu_0^2} = 10^6 \tag{37}$$

The fluid is assumed to be air with a constant Prandtl number of $Pr = 0.71$. The reference density ρ_0 is evaluated from the total mass of the air and the volume of the cavity. The length of the square's side, L, is taken as the reference length. The reference dynamic viscosity μ_0 is evaluated at the reference temperature of $T_0 = 600(K)$ using the Sutherland law for air

$$\frac{\mu}{\mu^*} = \left(\frac{T}{T^*}\right)^{3/2}\frac{T^* + 110.5}{T + 110.5} \tag{38}$$

with $T^* = 273(K)$ and $\mu^* = 1.68 \times 10^{-5}(kg/(m\ s))$. The thermal conductivity coefficient varies at the same rate of the dynamic viscosity coefficient to keep the local Prandtl number constant.

The reference velocity is defined as $u_{ref} = (gL(T_h - T_c)/T_0)^{1/2}$ from which the square of the Froude number may be calculated as $Fr^2 = u_{ref}^2/(gL) = (T_h - T_c)/T_0 = 2\epsilon$. Furthermore, with the reference velocity defined previously and the given Prandtl and Rayleigh numbers, the Reynolds number may be evaluated as $Re = (Ra/Pr)^{1/2} \simeq 1195$.

A non-uniform grid of 128^2 points with the following algebraic equation for the grid clustering near the walls is employed [33]

$$x_i = L\frac{(2\alpha + \beta)\left(\frac{\beta+1}{\beta-1}\right)^{\frac{\eta-\alpha}{1-\alpha}} + 2\alpha - \beta}{(2\alpha + 1)\left(1 + \left(\frac{\beta+1}{\beta-1}\right)^{\frac{\eta-\alpha}{1-\alpha}}\right)} \tag{39}$$

with $\alpha = 0.5$, $\beta = 1.1$, and η a uniform point distribution. In the calculation of Vierendeels *et al.* [26], a 1024^2 stretched grid with a maximum aspect ratio of 80 has been used.

The solution is integrated in time until steady state is reached. The profiles of the horizontal velocity along the vertical centerline and the vertical velocity along the horizontal centerline are shown in Figure 3. It should be noted that the reference velocity in the study of Vierendeels *et al.* [26] is equal to $u_{ref}^{Vier.} = (PrgL(T_h - T_c)/T_0)^{1/2}$, which differs from the one used in the present study by a factor of the square root of the Prandtl number. To have a proper comparison, the velocity profiles of [26] are adjusted and multiplied by a factor of $Pr^{1/2}$ in Figure 3.

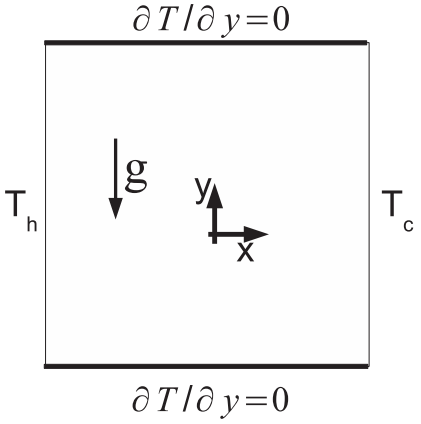

Figure 2. Sketch of the thermally driven square cavity.

DOI: 10.1002/fld

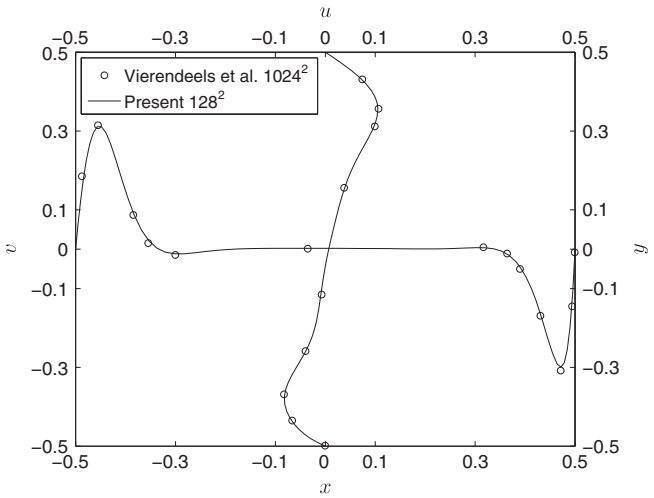

Figure 3. Velocity profiles along the centerlines of the thermally driven square cavity compared with the results of Vierendeels *et al.* [26].

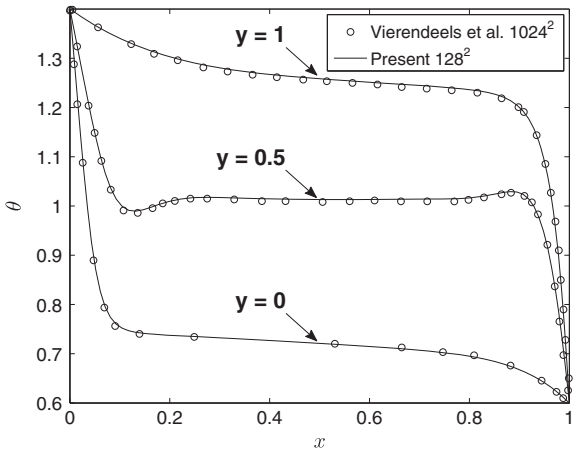

Figure 4. Temperature $\theta = (T - T_0)/T_0$ profiles along the top, bottom, and centerline of the thermally driven square cavity compared with the results of Vierendeels *et al.* [26].

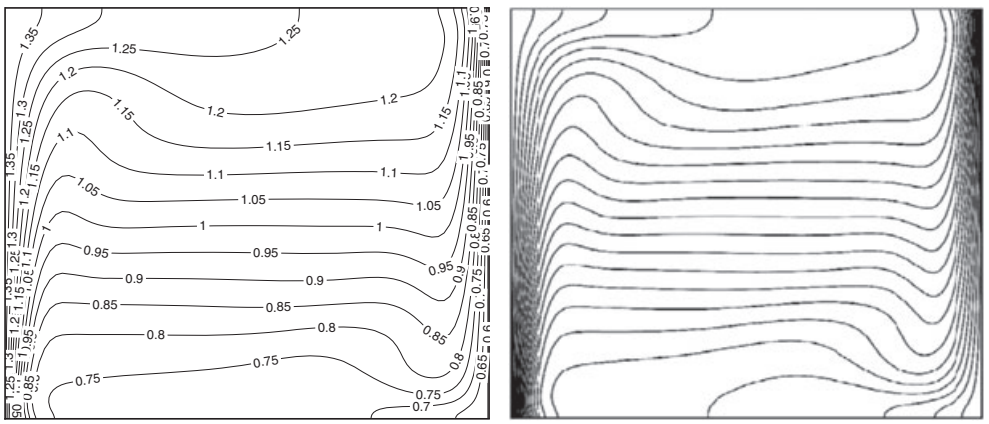

Figure 5. Contours of the temperature $\theta = (T - T_0)/T_0$ for the thermally driven square cavity, (left) present calculation, and (right) results of Vierendeels *et al.* [26].

DOI: 10.1002/fld

The variations of the temperature $\theta = (T - T_0)/T_0$ profiles along the adiabatic top and bottom walls, and also along the horizontal centerline, are presented in Figure 4. The contours of the temperature are given in Figure 5 and show a good qualitative agreement with the results of Vierendeels *et al.* [26]. Finally, the maximum and minimum values of the horizontal and vertical velocities, and also the average Nusselt numbers along the cold and hot walls are compared in Table I. In general, there is a good qualitative and quantitative agreement between the present results and the data of Vierendeels *et al.* [26].

4.2. Thermally driven inclined cavity

To test the ability of the method on non-orthogonal grids, the vertical walls of the square cavity shown in Figure 2 are inclined to the right at an angle of 45°. The temperature ratio and the non-dimensional temperature difference parameter are equal to $T_h/T_c = 1.02$ and $\epsilon = 0.01$, respectively. The temperature difference between the two walls is small, and the results can be compared with the data of Demirdzic *et al.* [27] obtained with the Boussinesq approximation. The Prandtl and Rayleigh numbers are equal to $Pr = 0.1$ and $Ra = 10^6$. A uniform grid of 256×256 points is used. The streamlines are shown in Figure 6. Three vortices are generated in the domain. One counter clockwise vortex is in the middle, and two clockwise vortices are above and below of the central vortex. The contours of the temperature, $(T - T_c)/(T_h - T_c)$, are shown in Figure 7, and the variations of the local Nusselt number along the cold wall are reported in Figure 8. In general, the agreement between the present results and the results of Demirdzic *et al.* [27] is very good.

Table I. Nusselt number and velocity comparison with the data of Vierendeels *et al.* [26].

	$\overline{\mathrm{Nu}}^{\mathrm{right}}$	$\overline{\mathrm{Nu}}^{\mathrm{left}}$	$u^{\max}_{x=0.5}$	$u^{\min}_{x=0.5}$	$v^{\max}_{x=0.5}$	$v^{\min}_{x=0.5}$
Present 128^2	8.743	8.743	0.1055	−0.0831	0.3102	−0.2994
Vierendeels *et al.* 1024^2	8.768	8.768	0.1070	−0.0832	0.3170	−0.3040

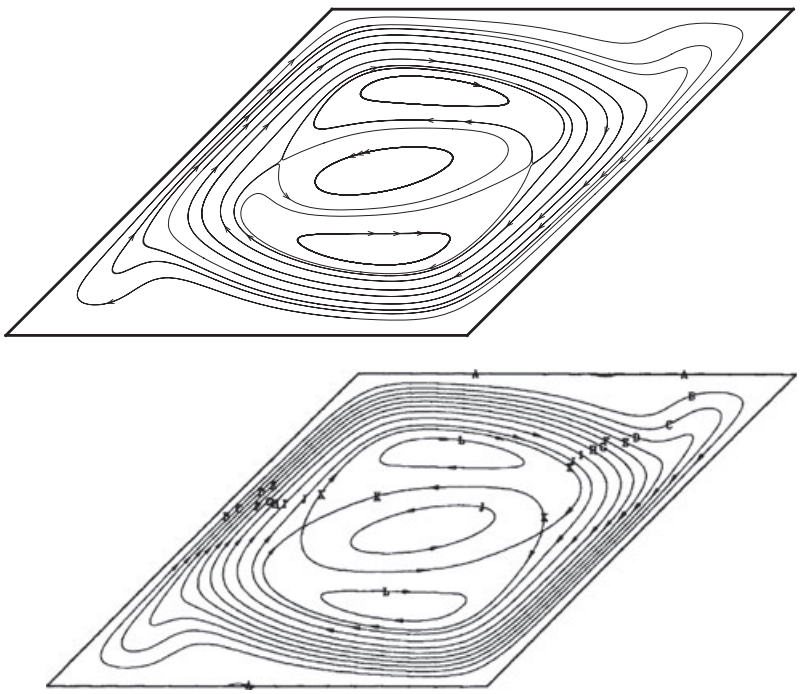

Figure 6. Streamlines of the thermally driven inclined cavity, (top) present calculation, and (bottom) results of Demirdzic *et al.* [27].

DOI: 10.1002/fld

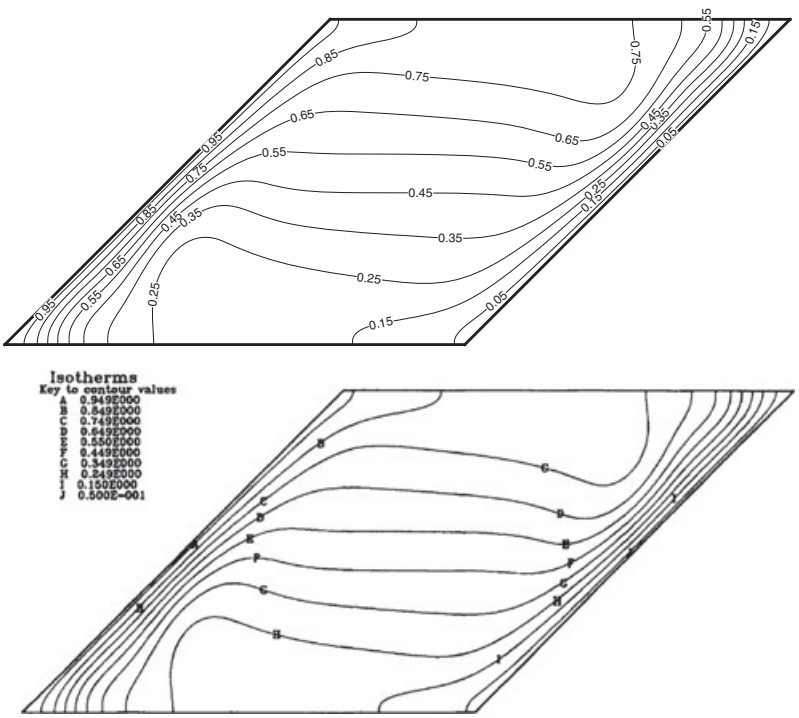

Figure 7. Contours of the temperature $(T - T_c)/(T_h - T_c)$ for the thermally driven inclined cavity, (top) present calculation, and (bottom) results of Demirdzic *et al.* [27].

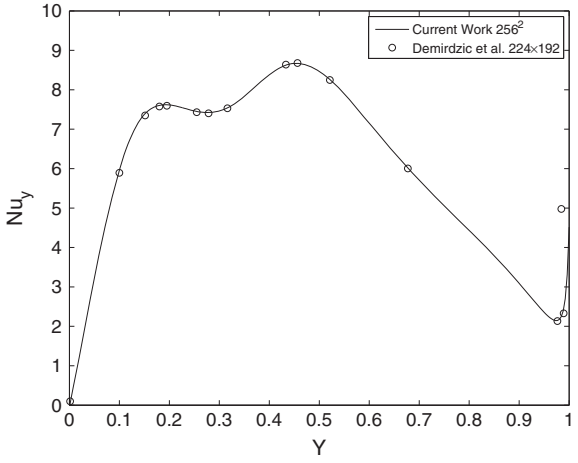

Figure 8. Variations of the local Nusselt number along the cold wall of the thermally driven inclined cavity compared with the results of Demirdzic *et al.* [27].

4.3. Lid-driven polar cavity

The geometry of the polar cavity with a clustered grid of 50×50 points is given in Figure 9. The non-uniform point distribution in the radial direction is obtained from Equation (39) with $\alpha = 0.5$ and $\beta = 1.1$. The outer to inner radius ratio is equal to $r_o/r_i = 2$. The flow is driven by the inner circle in the clockwise direction. The Reynolds number based on the azimuthal velocity of the inner circle, and the radius of the inner circle, is equal to $Re = 350$. The angle 2θ is equal to one radian, and the length of the inner arc is equal to r_i.

DOI: 10.1002/fld

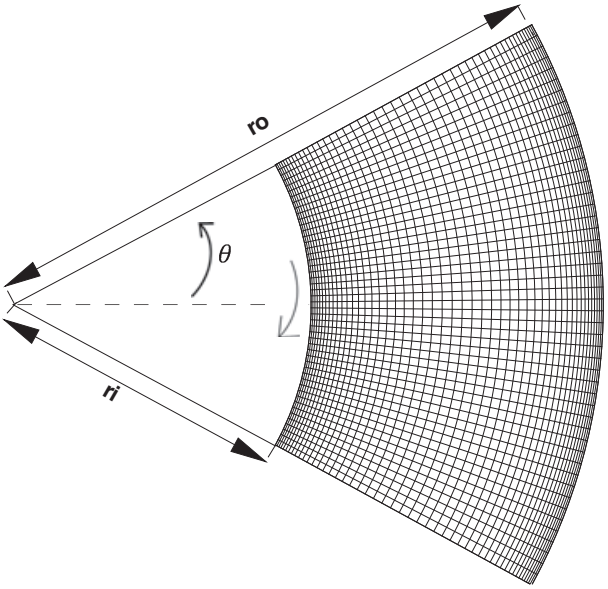

Figure 9. Geometry of the polar cavity with a non-uniform grid of 50×50 points.

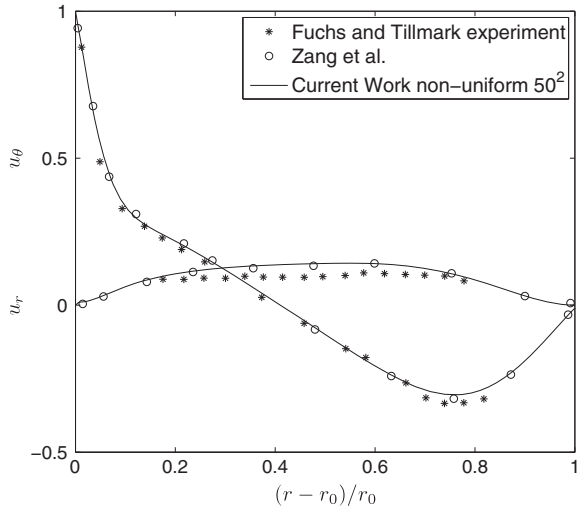

Figure 10. Azimuthal and radial velocity profiles along the radial line $\theta = 0$ compared with the experimental data of Fuchs and Tillmark [29], and the numerical results of Zang *et al.* [17].

The azimuthal and radial velocity profiles along the radial line $\theta = 0$ are compared with the experimental data of Fuchs and Tillmark [29] and the numerical results of Zang *et al.* [17] in Figure 10. There is small discrepancy between the present numerical and experimental results. The same amount of discrepancy is observed between the experimental data of Fuchs and Tillmark [29] and the numerical results of Zang *et al.* [17]. This difference, as explained in [17], may be attributed to the three-dimensional effects in the experiments of Fuchs and Tillmark [29]. The streamlines are compared with the numerical results of Zang *et al.* [17] in Figure 11. There is a good qualitative agreement between the streamlines regarding the location, shape, and size of the vortices. In Figure 11, the coordinates of the centers of the three vortices can be approximated as follows: $(x/r_i = 1.68, y/r_i = 0.72)$, $(x/r_i = 1.39, y/r_i = -0.17)$, and $(x/r_i = 1.66, y/r_i = -0.80)$ for the upper, middle, and lower vortex, respectively, where $(x = 0, y = 0)$ is the center of the circles.

DOI: 10.1002/fld

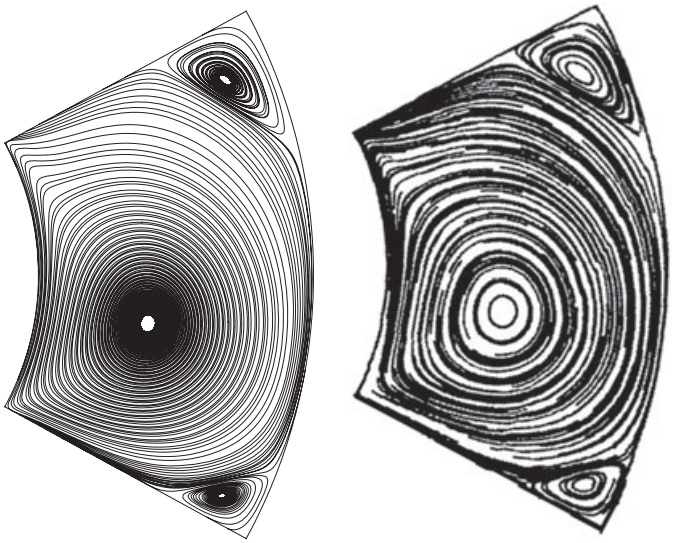

Figure 11. Streamlines of the lid-driven polar cavity. Left: present calculation and right: results of Zang *et al.* [17].

4.4. Three-dimensional lid-driven cavity

The three-dimensional lid-driven cavity problem has been numerically studied, among others, by Albensoeder and Kuhlmann [30] using an accurate Chebyshev spectral method. A grid of 64^3 points is used in three directions with a near wall clustering obtained from Equation (39) with $\alpha = 0.5$ and $\beta = 1.1$. The lid velocity is the reference velocity, and the side length of the square cavity is the reference length, both taken equal to one. The center of the system of coordinates is at the center of the cavity, and the flow is driven by the $x = -0.5$ wall in the positive y-direction. The profiles of the y-direction velocity, $v/2$, along the horizontal centerline $(x, 0, 0)$, and the profiles of the x-direction velocity, $u/2$, along the vertical centerline $(0, y, 0)$, are compared with the data of Albensoeder and Kuhlmann [30] in Figure 12 for two different values of the Reynolds number.

The streamlines are shown in Figure 13. They show the pathline of a fluid particle starting from the left wall moving in a spiral motion towards the center of the primary vortex from where it

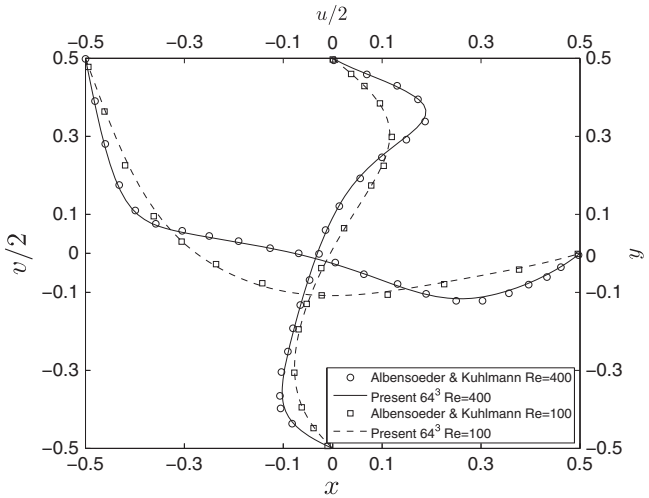

Figure 12. Profiles of the y-direction velocity, $v/2$, along the horizontal centerline $(x, 0, 0)$, and the x-direction velocity, $u/2$, along the vertical centerline $(0, y, 0)$, compared with the results of Albensoeder and Kuhlmann [30].

DOI: 10.1002/fld

subsequently rotates radially outward and finally returns to the left wall forming a closed particle path. The same trend has been observed in the study of Vahl Davis and Mallinson [34].

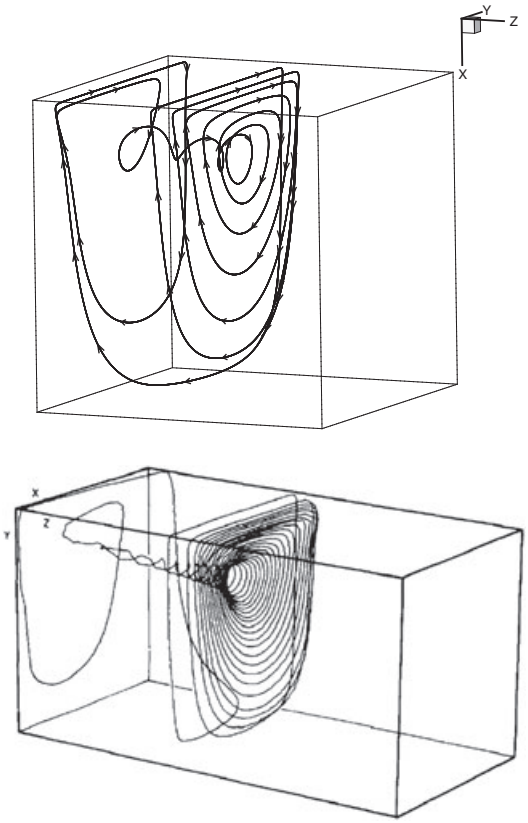

Figure 13. Streamlines of the three-dimensional lid-driven cavity (top) compared with the results of Vahl Davis and Mallinson [34] (bottom) showing the spiral shape of the streamlines.

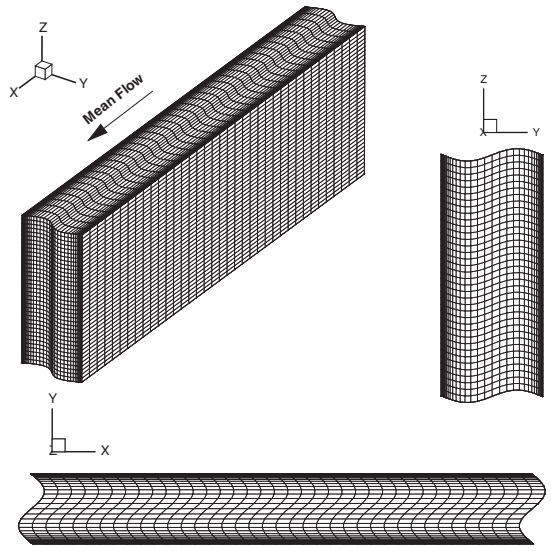

Figure 14. Geometry of the turbulent channel flow with non-orthogonal grid. Coarser grid than the actual one is shown for clarity.

DOI: 10.1002/fld

4.5. Turbulent channel flow

We consider the turbulent flow in a channel whose walls are kept in different temperatures. The schematic of the computational grid is shown in Figure 14. Coarser grid than that employed in the simulation is shown for clarity. In the simulation, a mesh of 128^3 points is used with a uniform distribution in the streamwise and spanwise direction, and a non-uniform hyperbolic tangent distribution in the wall-normal direction. The dimensions of the domain in the x, y, and z directions are, respectively, $l_x = 4\pi\delta$, $l_y = 2\delta$, and $l_z = 4/3\pi\delta$, with δ the channel half width. The initial Cartesian grid is distorted using a sine function with an amplitude of $0.03l_z$ in the spanwise direction and $0.03l_x$ in the streamwise direction. The channel walls are normal to the y-direction and are kept at constant temperature of T_c (cold) and T_h (hot), with a wall temperature ratio of $T_\mathrm{h}/T_\mathrm{c} = 2$. The boundaries of the domain normal to the x and z directions are periodic.

Table II. Comparison of flow parameters between the present simulation and the DNS of Nicoud and Poinsot [31, 32].

Case	$Re_{\tau\mathrm{h}}$–$Re_{\tau\mathrm{c}}$	$\left(B_{q\mathrm{h}} - -B_{q\mathrm{c}}\right)/10^{-2}$	$u_{\tau\mathrm{h}}/u_\tau$–$u_{\tau\mathrm{c}}/u_\tau$	$\left(C_{f\mathrm{h}} - -C_{f\mathrm{c}}\right)$ ‘$/10^{-3}$
Present	89–223	1.4–1.89	1.14–0.86	5.8–6.5
DNS [31, 32]	82–200	1.4–1.8	1.13–0.87	5.6–6.5

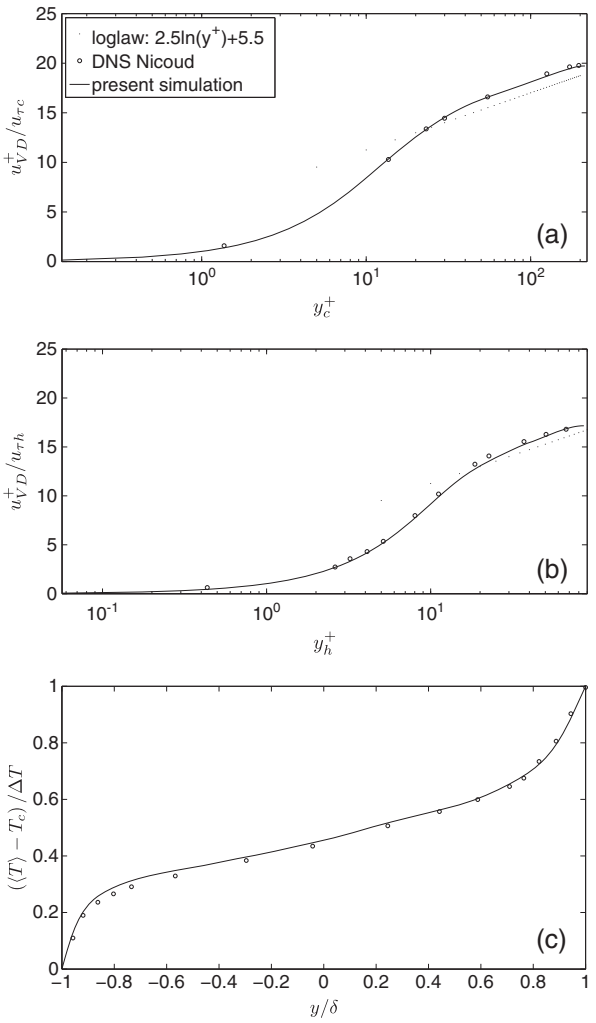

Figure 15. Mean velocity profiles with the van Driest transformation for (a) cold plate region, (b) hot plate region, and (c) mean temperature profile compared with the DNS of Nicoud [31].

DOI: 10.1002/fld

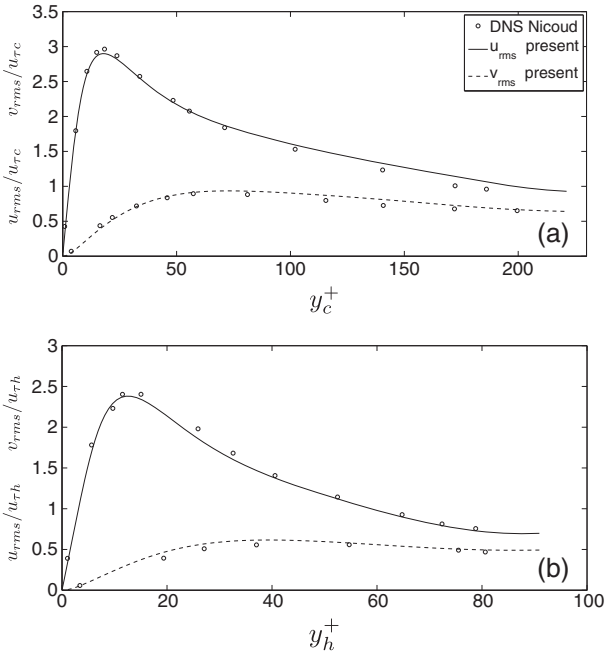

Figure 16. Streamwise and normal velocity fluctuations for (a) cold plate region and (b) hot plate region compared with the DNS of Nicoud [31].

The molecular Prandtl number is $Pr = 0.8$. The Reynolds number based on the channel half width δ, average friction velocity $u_\tau = (u_{\tau c} + u_{\tau h})/2$, bulk density ρ_b, and dynamic viscosity at the cold plate temperature μ_c is equal to $Re_\tau = \rho_b u_\tau \delta/\mu_c = 180$. The friction velocity at the cold wall is defined as $u_{\tau c} = (\tau_c/\rho_c)^{1/2}$, where τ_c is the shear stress, and ρ_c is the density at the cold wall. In the same way, the friction velocity at the hot wall, $u_{\tau h} = (\tau_h/\rho_h)^{1/2}$, is defined on the basis of hot wall values.

In Table II, the friction Reynolds numbers based on the cold and hot wall values ($Re_{\tau c} = \rho_c u_{\tau c}\delta/\mu_c, Re_{\tau h} = \rho_h u_{\tau h}\delta/\mu_h$) are given. The heat flux parameters on the cold and hot walls ($B_{qc} = q/(\rho_c c_p u_\tau T_c)$, $B_{qh} = q/(\rho_h c_p u_\tau T_h)$) as well as the friction coefficients ($C_{fh} = \tau_h/(\rho_b u_{max}^2/2)$, $C_{fc} = \tau_c/(\rho_b u_{max}^2/2)$) are also presented. In these equations, q is the wall heat flux, and u_{max} is the maximum streamwise velocity. The present results are in close agreement with the DNS results of Nicoud and Poinsot [31,32] performed on a $120 \times 100 \times 120$ grid points.

Figure 15 compares the mean velocity profiles near the cold and hot walls. Mean values are calculated by averaging in time and in planes parallel to the walls. The time averaging is performed for a time interval of $tu_\tau/\delta = 10$. The van Driest transformation expressed as $u_{VD}^+ = \int_0^{u^+} (\rho/\rho_w)^{1/2} du^+$, with ρ_w the fluid density at the wall, is applied to the velocity profiles. The velocity profile at the cold plate region is normalized with $u_{\tau c}$ and plotted versus the cold wall coordinates $y_c^+ = \rho_c u_{\tau c} y/\mu_c$ in Figure 15a. Similarly, in Figure 15b, $u_{\tau h}$ and $y_h^+ = \rho_h u_{\tau h} y/\mu_h$ are used at the hot plate region. The mean temperature profile is compared in Figure 15c. The streamwise and normal velocity fluctuations at the cold and hot plate regions are compared in Figure 16a and 16b, respectively.

5. CONCLUSIONS

In this article, a robust algorithm for time-accurate calculations of low-Mach number, variable density flows in general curvilinear coordinates has been presented. Instead of the more popular staggered grid, the collocated grid arrangement has been used. The advantage of the collocated grid arrangement over the staggered grid arrangement is its computational simplicity in three-dimensional curvilinear coordinates. To avoid the odd–even decoupling problem of the collocated

DOI: 10.1002/fld

grids, the flux interpolation technique is generalized to variable-density flows. To increase the stability of the solver at high-temperature differences, a two-stage predictor–corrector time marching method has been used. The robustness and accuracy of the algorithm has been assessed through simulations of five well-known test problems. The results with the proposed algorithm are in very good agreement with the ones reported earlier.

ACKNOWLEDGEMENTS

The authors would like to thank Prof. Mohsen Bahrami and Mr. Nima Tofighi at Amirkabir University of Technology, Iran for several helpful discussions during the preparation of this manuscript.

REFERENCES

1. Turkel E. Preconditioning techniques in computational fluid dynamics. *Annual Reviews in Fluid Mechanics* 1999; **31**:385–416.
2. Weiss JM, Smith WA. Preconditioning applied to variable and constant density flows. *AIAA Journal* 1995; **33**:2050–2057.
3. Corvellec C, Bruel P, Sabel'Nikov VA. A time-accurate scheme for the calculations of unsteady reactive flows at low Mach number. *International Journal for Numerical Methods in Fluids* 1999; **29**:207–227.
4. Lessani B, Ramboer J, Lacor C. Efficient large-eddy simulations of low Mach number flows using preconditioning and multigrid. *International Journal of Computational Fluid Dynamics* 2004; **18**:221–233.
5. Majda A, Sethian J. The derivation and numerical solution of the equations for zero Mach number combustion. *Combustion Science and Technology* 1985; **42**:185–205.
6. de Charentenay J, Thévenin D, Zamuner B. Comparison of direct numerical simulations of turbulent flames using compressible or low Mach number formulations. *International Journal for Numerical Methods in Fluids* 2002; **39**:497–515.
7. Cook AW, Riley JJ. Direct numerical simulation of a turbulent reactive plume on a parallel computer. *Journal of Computational Physics* 1996; **129**:263–283.
8. Najm HN, Wyckoff PS, Knio OM. A semi-implicit numerical scheme for reacting flows, I. stiff chemistry. *Journal of Computational Physics* 1998; **143**:381–402.
9. Schneider Th, Botta N, Geratz KJ, Klein R. Extension of finite volume compressible flow solvers to multi-dimensional, variable density zero Mach number flow. *Journal of Computational Physics* 1999; **155**:248–286.
10. Nicoud F. Conservative high-order finite-difference schemes for low-Mach number flows. *Journal of Computational Physics* 2000; **158**:71–97.
11. Lessani B, Papalexandris MV. Time-accurate calculation of variable density flows with strong temperature gradients and combustion. *Journal of Computational Physics* 2006; **212**:218–246.
12. Lessani B, Papalexandris MV. Numerical study of turbulent channel flow with strong temperature gradients. *International Journal of Numerical Methods for Heat and Fluid Flow* 2008; **18**:545–556.
13. Pierce ChD. Progress-variable approach for large-eddy simulation of turbulent combustion. *Ph.D. Thesis*, Stanford University, 2001.
14. Sewall EA, Tafti DK. A time-accurate variable property algorithm for calculating flows with large temperature variations. *Computers & Fluids* 2008; **37**:51–63.
15. Rauwoens P, Vierendeels J, Merci B. A solution for the odd-even decoupling problem in pressure-correction algorithms for variable density flows. *Journal of Computational Physics* 2007; **227**:79–99.
16. Harlow FH, Welch JE. Numerical calculation of time-dependent viscous incompressible flow of fluid with free surface. *Physics of Fluids* 1965; **8**:2182–2189.
17. Zang Y, Street RL, Koseff JR. A non-staggered grid, fractional step method for time-dependent incompressible Navier–Stokes equations in curvilinear coordinates. *Journal of Computational Physics* 1994; **114**:18–33.
18. Rhie CM, Chow WL. A numerical study of the turbulent flow past an airfoil with trailing edge separation. *AIAA Journal* 1983; **21**:1525–1532.
19. Morinishi Y, Lund TS, Vasilyev OV, Moin P. Fully conservative higher order finite difference schemes for incompressible flow. *Journal of Computational Physics* 1998; **143**:90–134.
20. Armenio V, Piomelli U. A Lagrangian mixed subgrid-scale model in generalized coordinates. *Flow, Turbulence and Combustion* 2000; **65**:51–81.
21. Moulinec C, Wesseling P. Collocated schemes for the incompressible Navier–Stokes equations on non-smooth grids for two-dimensional problems. *International Journal for Numerical Methods in Fluids* 2000; **32**:349–364.
22. Jothiprasad G, Caughey DA. A collocated, iterative fractional-step method for incompressible large eddy simulation. *International Journal for Numerical Methods in Fluids* 2008; **58**:355–380.
23. Gopalakrishnan P, Tafti DK. A parallel boundary fitted dynamic mesh solver for applications to flapping flight. *Computers & Fluids* 2009; **38**:1592–1607.
24. Lessani B, Zainali A. Numerical investigation of stably stratified turbulent channel flow under non-Boussinesq conditions. *Journal of Turbulence* 2009; **10**:1–25.

DOI: 10.1002/fld

25. Tannehill JC, Anderson DA, Pletcher RH. *Computational fluid mechanics and heat transfer*. Hemisphere: New York, 1984.
26. Vierendeels J, Merci B, Dick E. Benchmark solutions for the natural convective heat transfer problem in a square cavity with large horizontal temperature differences. *International Journal of Numerical Methods for Heat and Fluid Flow* 2003; **13**:1057–1078.
27. Demirdzic I, Lilek Z, Peric M. Fluid flow and heat transfer test problems for non-orthogonal grids: benchmark solutions. *International Journal for Numerical Methods in Fluids* 1992; **15**:329–354.
28. Cheng YP, Lee TS, Low HT. An efficient and robust numerical scheme for the SIMPLER algorithm on non-orthogonal curvilinear coordinates: CLEARER. *Numerical Heat Transfer, Part B* 2007; **51**:433–461.
29. Fuchs L, Tillmark N. Numerical and experimental study of driven flow in a polar cavity. *International Journal for Numerical Methods in Fluids* 1985; **5**(4):311–329.
30. Albensoeder S, Kuhlmann HC. Accurate three-dimensional lid-driven cavity flow. *Journal of Computational Physics* 2005; **206**:536–558.
31. Nicoud F. Numerical study of a channel flow with variable properties, Center for Turbulence Research (CTR) Annual Research Briefs, Stanford 1998:289–310.
32. Nicoud F, Poinsot T. DNS of a channel flow with variable properties. *First International Symposium on Turbulence and Shear Flow Phenomena (TSFP-1)*, Santa Barbara, 1999.
33. Hofmann KA, Chiang S T. Computational fluid dynamics, Engineering Education System 2000.
34. Vahl Davis G, Mallinson GD. An evaluation of upwind and central difference approximation by a study of recirculating flow. *Computers & Fluids* 1976; **4**:29–43.

DOI: 10.1002/fld